

Focus Quality Assessment of High-Throughput Whole Slide Imaging in Digital Pathology

Mahdi S. Hosseini, *Member, IEEE*, Jasper A. Z. Brawley-Hayes, Yueyang Zhang, Lyndon Chan, *Student member, IEEE*, Konstantinos N. Plataniotis, *Fellow, IEEE*, and Savvas Damaskinos

Abstract—One of the challenges facing the adoption of digital pathology workflows for clinical use is the need for automated quality control. As the scanners sometimes determine focus inaccurately, the resultant image blur deteriorates the scanned slide to the point of being unusable. Also, the scanned slide images tend to be extremely large when scanned at greater or equal 20X image resolution. Hence, for digital pathology to be clinically useful, it is necessary to use computational tools to quickly and accurately quantify the image focus quality and determine whether an image needs to be re-scanned. We propose a no-reference focus quality assessment metric specifically for digital pathology images, that operates by using a sum of even-derivative filter bases to synthesize a human visual system-like kernel, which is modeled as the inverse of the lens' point spread function. This kernel is then applied to a digital pathology image to modify high-frequency image information deteriorated by the scanner's optics and quantify the focus quality at the patch level. We show in several experiments that our method correlates better with ground-truth z -level data than other methods, and is more computationally efficient. We also extend our method to generate a local slide-level focus quality heatmap, which can be used for automated slide quality control, and demonstrate the utility of our method for clinical scan quality control by comparison with subjective slide quality scores.

Index Terms—no-reference focus quality assessment, whole slide imaging, digital pathology, out-of-focus heatmap, human visual system, MaxPol derivative library

I. INTRODUCTION

CLINICAL pathology is witnessing a paradigm shift by transferring from glass tissue slides (observed by optical microscopy) to digital slides scanned with whole slide imaging (WSI) systems. WSI scanners generate high resolution (submicron) images that can aid in the diagnosis of disease by permitting convenient visualization and navigation of tissue slide images. In clinical pathology departments, hundreds to thousands of tissue slides are processed each day and the number of cases has been steadily increasing, creating a challenging workload for digital pathology [1].

Copyright (c) 2019 IEEE. Personal use of this material is permitted. However, permission to use this material for any other purposes must be obtained from the IEEE by sending a request to pubs-permissions@ieee.org.

M. S. Hosseini, Y. Zhang, L. Chan and K. N. Plataniotis are with The Edward S. Rogers Sr. Department of Electrical and Computer Engineering, University of Toronto, Toronto, ON M5S 3G4, Canada e-mail: mahdi.hosseini@mail.utoronto.ca.

M. S. Hosseini, J. A. Z. Brawley-Hayes, are S. Damaskinos are with Huron Digital Pathology Inc., St. Jacobs, ON N0B 2N0, Canada.

This paper has supplementary downloadable material available at <https://github.com/mahdihosseini/FQPath> provided by the authors. The material includes MATLAB package for No-Reference (NR) Focus Quality Assessment (FQA) of Digital Pathology Images.

Routine diagnosis of pathology slides requires high quality high-throughput images, which are directly affected by the dynamic environment of the physical optics and sensor electronics of the scanner [2]–[4].

High quality images from the slides must be displayed in a consistent and reliable manner to assist pathologists in interpreting these images accurately and efficiently. However, existing digital pathology solutions still face challenges. For example, many WSI scanners need a manual inspection of digital slides for focus quality control (FQC), which is a tedious and laborious task. In high-throughput scanning systems, which contain hundreds of slides for processing, making it impractical to perform a manual FQC check for each individual slide. A robust, highly reliable automated solution (“one-click” mode) would eliminate the need for manual FQC checking, and make the integrated imaging software more user friendly. The computational complexity of any automated FQC assessment technique should also be compatible with widely available scanning platforms, without the requirement of custom hardware. It can be a cost effective solution for digital pathology departments.

In discrete computational modeling, there exist several no-reference (NR) focus quality assessment (FQA) (together called NR-FQA) metrics that can be applied in synthetic or natural imaging applications for sharpness assessment such as using gradient map [5]–[9], contrast map [10]–[12], phase coherency [13], [14], and deep learning solutions [15]–[17]. Please refer to [18] and the references therein for more information on the methodologies. The performance accuracy of these metrics is usually evaluated by comparison with the subjective scores of a test database where the blur level of the image is scored by an individual subject. This score is correlated with the objective scores provided by NR-FQA metric for accuracy measurement. Despite their effectiveness for synthetic blur assessment, the correlation accuracy of such methods is usually low for naturally blurred images, partly because such images are usually captured in different blurring types, various scales, and illumination conditions. Beyond such irregularities, high accuracy NR-FQAs in the literature are highly complex in terms of computational speed, which makes them impractical for real-time applications.

The general application of NR-FQA metrics developed for blurred images is different from out-of-focus blur in digital pathology. In fact, when it comes to digital pathology, imaging is done in a controlled environment where (a) the magnification is consistent through the image, with most manufacturers using a similar pixel pitch, (b) image uniformity is controlled by

the quality of illumination optics to uniformly distribute light at the tissue located at the focal plane of the objective lens, and (c) poor focusing is the dominant factor of image blur in scanned images while image blur caused by motion of slide in the direction of scan is comparatively very small. Various methods take advantage of the scan control environment to employ simplified approaches for NR-FQA development in digital pathology. To meet the needs for efficiency and fast computational speed, these methods employ statistical measurements for feature extraction that are related to absolute image blurriness. For detailed review of these methods please refer to [19]–[26] and references therein. More advance techniques have been also deployed by different vendors of WSI systems to obtain the focus positions in real-time for auto-focusing such as using the Optical Coherence Tomography (OCT) imaging systems in ThorLabs¹, second tilted sensor in Philips' system [27], deploying a second sensor in forth and back motion in GE's system [28], Transform and multi-domain deep learning solution in [29], and the pre-determined focus map in Huron's system².

Analysis of blur using such methods is highly effective for calculating the relative difference between images where structural similarity is preserved across different focus levels, known as the in-depth Z-stacks [30]. However, using statistical measurements for focus quality assessment of image patches at the whole slide level is a challenge. The diversity of both structures (tissue morphology patterns) and focus quality levels across different positions in WSIs makes NR-FQA metric development a hard problem to solve. It is note worthy that all scanner manufacturers have problems with focusing. The focus failures are present regardless of the focus method – be it pre-focus map, stop and stare, or real-time autofocusing. Additionally, even if a perfect scanner system were to be created, the sample itself can have folds or bubbles or other causes of discontinuity, which make a perfectly focused image from a single surface impossible. Post-acquisition focus quality assessment methods, will always be relevant as hardware and software can always have faults (manufacturer defect, bug, mis-use, wear, etc). In fact, very few methods exist in the literature to address NR-FQA so as to create a local quality map (like a heatmap) to reliably assess the in-focus vs out-of-focus regions in a WSI. Recent developments tend to solve this problem either by statistical regression of blur features [26], [31], [32] or by developing a deep-learning solution with convolutional neural networks (CNNs) [33]. Unfortunately, the lack of (a) generalization to a broad spectrum of tissue types and (b) computational efficiency are the main drawbacks of such methodologies. This makes the NR-FQA still an unresolved problem in digital pathology for focus quality assessment in WSI.

We propose an NR-FQA metric called FQPath³ which extracts focus-related features from a digital pathology image that requires no prior knowledge from the user for reliable analysis of the blur levels to (a) grade the image quality across

different patches in a WSI and (b) grade the WSI scan quality across slides of different tissue types. The key idea behind our solution is the synthesis of a convolution filter using the MaxPol derivative kernel library [34], [35], that mimics the human visual system response for microscopy applications in order to equalize the frequency spectrum of the image for blur feature extraction. We use this feature to develop our NR-FQA metric which is a variant of the method detailed in a previous paper for general-application NR-FQA [36]. The proposed NR-FQA metric i.e. FQPath extracts features with this synthesized kernel instead of fixed derivative kernels, and accuracy is measured by correlation with scanning z-level instead of subjective score.

In this paper, we make the following contributions to improving WSI in digital pathology:

- We develop a novel method for measuring how close the specimen was to the object plane at the time of acquisition using a NR-FQA. This method is based on the human visual system's characteristic equalization of spatial frequency expression in an image, which allows us to distinguish between subtle changes in sharpness as a result of defocusing.
- We leverage the NR-FQA metric to generate a focus quality heatmap of whole slide images by applying the metric on small image patches. We propose an inverse Gaussian mapping of the metric scores to further improve the usability of the heatmap.
- We introduce a database of 200 WSI scans of histology slides stained with H&E containing a variety of tissue types. From these images, we create a subjective scoring protocol to grade the focus quality at the WSI level.
- We conduct two sets of experiments to (a) compare ten state-of-the-art NR-FQA metrics based on their correlation to actual z-level; and (b) provide a quality control tool to aid in rapid grading of the focus level of WSI scans and provide the means to define a pass/fail threshold based on subjective scoring of images.

Our early related works [18], [36] propose no-reference image sharpness assessment methods that were designed for general purposes of both synthetic and natural imaging applications to grade the image quality with respect to diverse spectrum of blur information. In this paper, we introduce a metric that is mainly tailored for microscopic blur image analysis applied in digital pathology to grade the out-of-focus levels of both image patch and slide levels.

The work accomplished in this paper is described in sections below as follows. In Section II we introduce the concept of HVS convolution kernel synthesis based on out-of-focus imaging in optical microscopy. In Section III we adopt the HVS convolution kernel and propose an NR-FQA metric that we apply on digital image patches. In Section IV we construct a focus quality heatmap of WSI scans while in Sections V and VI we describe two sets of experiments to validate the proposed approach of focus quality assessment of digital pathology images. Finally, conclusions and recommendations are presented in Section VII.

¹https://www.thorlabs.com/navigation.cfm?guide_id=2039

²<http://www.hurondigitalpathology.com/tissuescope-le-3-2/>

³<https://github.com/mahdihosseini/FQPath>

II. HUMAN VISUAL RESPONSE-MICROSCOPY LIKE KERNEL SYNTHESIS

In this section, we explain our approach to model the out-of-focus characteristics of a digital pathology scanner that is caused by focal depth offset between the tissue slide and the scanner's objective lens. In particular, we synthesize a human visual system (HVS)-like kernel for optical microscopy (called HVS-Microscopy, or HVS-M for short) from derivative basis filters. This HVS-M kernel is then used to partly correct the high-frequency fall-off in the scanned image's amplitude response caused by the microscope's optics being out-of-focus relative to the plane of the sample. The corrected image is used to extract focus quality-related features.

A. Out-of-Focus in WSI Scanning System

One common practice in whole slide imaging (WSI) to determine the focus map of a tissue specimen on a glass slide is to pre-measure the focus positions at several locations on the slide and interpolate a surface that passes through the measured focus points. This is accomplished with a fast low-resolution ($\leq 1X$) preview scan of the whole tissue slide. A region or regions-of-interest (ROIs) are defined to be scanned at high-resolution ($\geq 20X$). Within these regions (or a single region), a set of focus points are defined on the tissue. At each point, the scanner will perform a through-focus scan, typically a volume image, from which one lateral dimension may be discarded. The resulting xz-scans or xy-scans (one from each focus point) are run through an algorithm to determine the row or column of the image corresponding to the sample being at best focus. Since the image capture was synchronized with a stage encoder, the focus positions can be determined from these images. Using the known (x_i, y_i) coordinates of each measurement of z_i , a surface can be interpolated through all measured points. This interpolated surface is used to compute the optimal z position for each frame during final high-resolution image acquisition.

During acquisition, errors may occur, which can lead to some or all parts of the image being out of focus. Some of these factors may be:

- thermal effects in the mechanical system, which affect the repeatability of the position of the sample in relation to the indicated encoder value
- internally or externally generated vibration
- errors in the focus determination algorithm
- errors in the generation of the focus map
- insufficient number of focus points to define an accurate focus map
- errors in tissue preparation, such as folds or lifting off the slide surface

These factors cause the sample to pass either above or below the object plane of the objective lens, which leads to a blurred image at the camera sensor. In our approach, we attempt to quantify the image quality deterioration based on defocus, which may be caused by any of these factors. Examples of different source cause of such factors are shown in Figure 1.

In optical microscopy, the point spread function (PSF) describes a general diffraction model of the optical spreading, for both in-focus and out-of-focus behavior, that results when

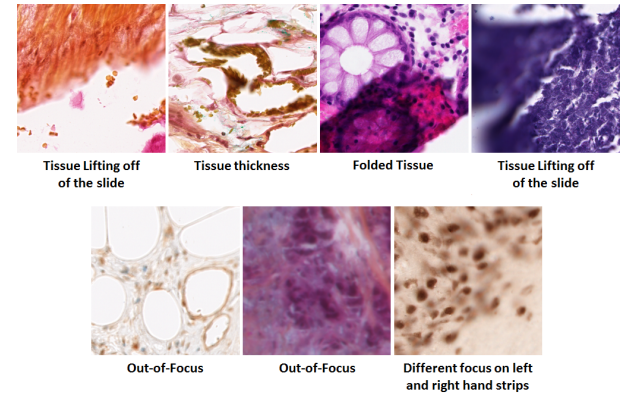


Fig. 1. Image patch examples of variants of out-of-focus causing by different different factors such as tissue preparation issues and scanning error.

a focused imaging lens is (by definition) aligned with the target specimen in the lateral plane, i.e. (X,Y) coordinates, but not necessarily along the optical axis, i.e. Z coordinate. For different focal depth offsets (Z) from the optimal value, a different lateral characteristic will be observed. We chose to model the digital pathology scanner optical characteristic using the Born & Wolf model [37].

$$h_{PSF}(r, z) = \left| C \int_0^1 J_0(k \frac{NA}{n} r \rho) e^{-\frac{1}{2} ik \rho^2 z (\frac{NA}{n})^2} \rho d\rho \right|^2 \quad (1)$$

where,

r - the radial distance from the optical axis along the lateral plane ($r = \sqrt{x^2 + y^2}$, where x and y are the lateral Cartesian coordinates)

z - the distance between the imaging plane and the in-focus position along the optical axis

C - a normalization constant

J_0 - zero-order Bessel function of the first kind

k - angular wavenumber of the lightsource ($k = \frac{2\pi}{\lambda}$)

NA - the numerical aperture of the objective lens

n - the refractive index of the medium

i - the imaginary number

ρ - the normalized coordinate in the exit pupil.

In Figures 2(a) and 2(b), we show a mathematical model of the PSF function using Equation 1 in the axial plane (YZ) at two different x -levels. When the objective lens is in focus with respect to lateral plane X i.e. $x = 0$, the extent of the frequency domain-PSF is much wider in the y -direction than when the x -level is out-of-focus $x = 4$, shown in Figures 2(e) and 2(f). This shows the importance of proper lateral alignment of the objective lens to mitigate lateral diffraction.

In Figures 2(c) and 2(d), we show the PSF in the lateral plane (XY) at two different z -levels. Note that the lens is in-focus along the optical axis when the z -level is zero, causing the model to contain only optical aberration (mainly wavefront) effects. A non-zero z -level corresponds to an out-of-focus lens along the optical axis, causing the model to contain both optical aberration and out-of-focus effects. The frequency plots are also shown in Figures 2(g) and 2(h).

The corresponding one-dimensional PSF models are also shown in Figure 3 where they are taken along $y = 0$ (indicated

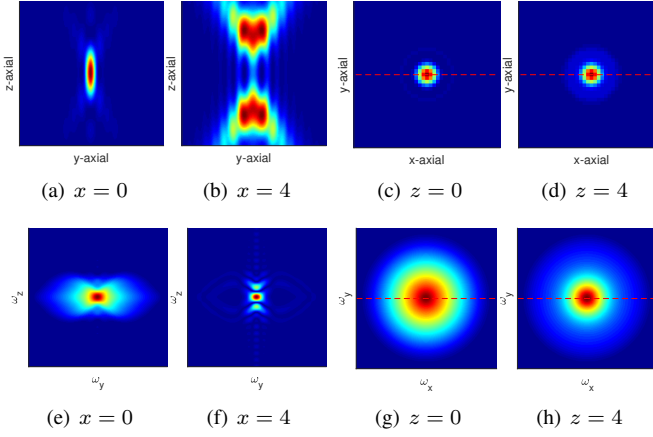


Fig. 2. 2D Plots of the PSF model defined in 1, displayed at different x- and z- cut levels shown in both the spatial i.e. first row from (a)-(e) and frequency domains i.e. second row from (e)-(h)

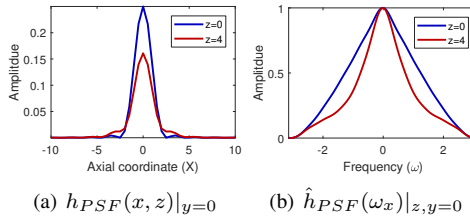


Fig. 3. The corresponding 1D PSF models taken along $y = 0$ (see the red dashed lines from z-cuts in Figure 2) from the 2D models are: (a) $z \in \{0, 4\}$ in spatial domain, (b) $z \in \{0, 4\}$ in frequency domain.

by the dotted red line) from the two-dimensional models shown in Figure 2. Note how the one-dimensional spatial-domain PSF is limited in amplitude for the out-of-focus case (i.e. $z \neq 0$) compared to the in-focus case ($z = 0$).

B. HVS-M Kernel Design

In the overall digital pathology process, the PSF described in 1 i.e. h_{PSF} can be seen as a low-pass filter (LPF) applied to a natural image, causing its high-frequency components to attenuate and appear blurred. It is also known [38]–[40] that the human visual system (HVS) uses a visual sensitivity response to boost the high frequency response of an image that can be seen as a deblurring operation. See Figure 4 for a diagram of this process.

Inspired by the human visual system's high-frequency-boosting behavior, we propose to synthesize a HVS-like kernel to reverse the high-frequency attenuating behavior in digital pathology images resultant from the PSF of the scanner. We hypothesize that, by boosting the high-frequency information of a scanned digital pathology image that is known to characterize image focality, we will be able to characterize the overall image focus quality.

Here, we design a frequency-equalizing kernel $h_{\text{HVS-M}}$ to mimic the behavior of the human visual system in boosting the high-frequency information attenuated by the modeled PSF:

$$h_{\text{PSF}}(r, z^*) * h_{\text{HVS-M}}(r) = \delta(r), r \in [-r_{\max}, r_{\max}]. \quad (2)$$

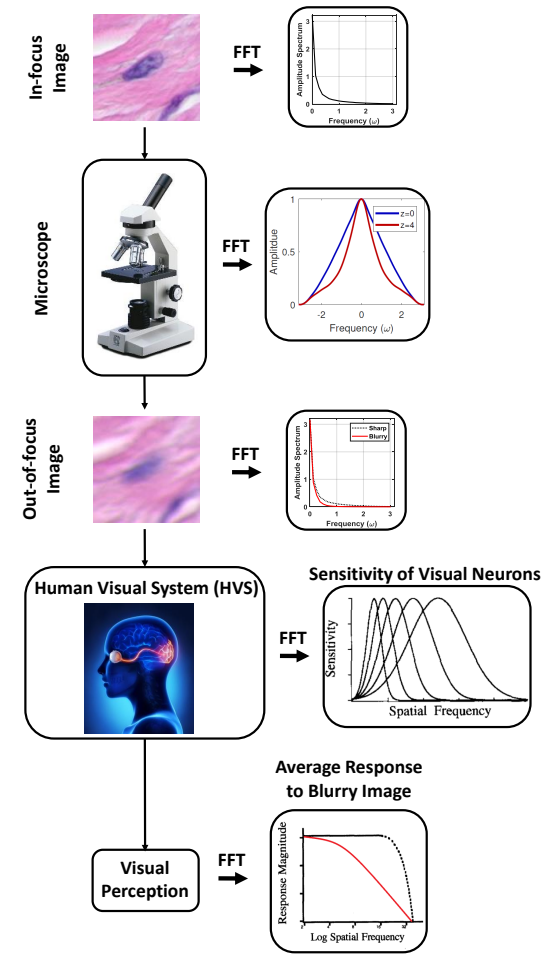


Fig. 4. Out-of-focus blurry microscopy image observed by the human visual system (HVS). The in-focus image of a tissue specimen has a high frequency fall-off characteristic, which is further aggravated by the PSF response of the microscope. The human visual system is known to boost the high-frequency information and perform a deblurring operation, and our synthesized HVS-M kernels are designed to mimic this behavior.

Note that z^* is the optimal microscope objective focal length where by accurate adjustment of this distance we count for both out-of-focus blur and natural image frequency falloff behavior. In particular, we are interested in balancing the frequency falloff in a bounded Fourier transform domain

$$\hat{h}_{\text{HVS-M}}(\omega) = \hat{h}_{\text{PSF}}(\omega, z^*)^{-1}, \omega \in [-\omega_c, \omega_c]. \quad (3)$$

We model such an enhancement by defining the HVS filter as a linear combination of even-derivative operators

$$h_{\text{HVS-M}}(r, z^*) \equiv \sum_{n=1}^N c_n d_{2n}(r) \quad (4)$$

where $d_{2n}(r) = d^{2n}/dr^{2n}$ is the $2n$ th derivative operator. The Fourier transform of the model in 4 gives

$$\hat{h}_{\text{HVS-M}}(\omega, z^*) = \sum_{n=1}^N c_n \hat{d}_{2n}(\omega) = \sum_{n=1}^N (-1)^n c_n \omega^{2n}. \quad (5)$$

The unknown coefficients $\{c_n\}_{n=1}^N$ are determined by fitting the response 5 to the inverse of the modeled PSF up to a threshold frequency ω_t

$$\underset{\{c_n\}_{n=1}^N}{\operatorname{argmin}} \|\hat{h}_{PSF}^{-1}(\omega) - \sum_{n=1}^N c_n (-1)^n \omega^{2n}\|_2, \omega \in [0, \omega_t]. \quad (6)$$

This threshold is defined such that to avoid fitting instability on high frequency bands ($\hat{h}_{PSF}^{-1}(\omega) \leq 30$ in our design case).

Once the optimum coefficients $\{c_n^*\}_{n=1}^N$ are obtained from 6, we construct the discrete model to the filter design in 5. We synthesize the even-order derivative filters \hat{d}_{2n} as low-pass filters up to a cutoff frequency ω_c (in order to balance fitting spurious high-frequency noise and retaining useful high-frequency information) using the MaxPol filter library solution [34], [35] which is optimized to approximate

$$\hat{d}_{2n}(\omega) \approx \begin{cases} (-1)^n \omega^{2n}, & 0 \leq \omega \leq \omega_c \\ 0, & \omega \geq \omega_c \end{cases}. \quad (7)$$

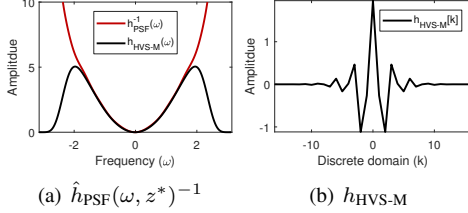


Fig. 5. Approximation of HVS-M kernel using MaxPol filter library solution. The optimal coefficients $\{c_n^*\}_{n=1}^N$ are approximated and used to weigh the linear combination of MaxPol even derivative kernels for inverse kernel reconstruction. The inverse spectrum $\hat{h}_{PSF}(\omega, z^*)^{-1}$ shown above corresponds to the PSF shown in Figure 3 for $z = 4$.

Figure 5 demonstrates an example of an approximated HVS-M kernel. The inverse profile $\hat{h}_{PSF}(\omega, z^*)^{-1}$ is first fitted by the frequency polynomials defined in (6), and the optimal coefficients $\{c_n^*\}_{n=1}^7$ are attained. These coefficients are used to combine different MaxPol even-derivative filters to construct the HVS-M kernel. All of the MaxPol filters are regulated by a cutoff frequency $\omega_c = 2$ for discrete approximation.

III. PATCH-BASED LEVEL FOCUS QUALITY ASSESSMENT

The constructed HVS-M kernel defined in the previous section can now be applied as a convolution operation to partly modify the frequency amplitudes of an out-of-focus image in order to extract sharpness features for focus quality grading in WSI image patch. The HVS-M kernel provides a meaningful transformation where the edge features across a wide frequency spectrum are balanced and become comparable with each other, and are known to be related to focus quality. Furthermore, by assigning a single focus quality score for each patch enables localized focus quality heatmap generation described in the next section.

The algorithmic framework of (a) synthesizing the HVS-M kernel, and (b) scoring focus quality of an image patch, are demonstrated in Algorithms 1 and 2, respectively. The linear coefficients for the synthesized HVS-M filter are first learned as a preliminary step in Algorithm 1 by minimizing

the L2 norm between the synthesized HVS-M filter and the modeled PSF filter. This is done by fitting the inverse PSF in the frequency domain with frequency polynomials up to the N th order to obtain the optimized coefficients $\{c_n^*\}_{n=1}^N$. Then, the coefficients are used to weight the linear combination of one-dimensional MaxPol lowpass derivative filters for synthesizing the HVS-M filter.

Algorithm 1: HVS-M Filter Synthesis

Data:

Out-of-Focus Microscopy PSF $h_{PSF}(z^*) \in \mathbb{R}^{2r_{max}+1}$, optimal parameters $\{z^*, \omega_c^*\}$

Result:

Synthesized FIR kernel $h_{HVS\text{-}M}$

1 Synthesize coefficients $\{c_n^*\}_{n=1}^N$ from (6)

2 Construct HVS-M by MaxPol lowpass derivative

$$\text{kernels } h_{HVS\text{-}M}[k] = \sum_{n=1}^N c_n^* d_{2n}[k]$$

Provided by the synthesized HVS-M kernel, we develop the focus metric in Algorithm 2. Our metric requires the input image patch to be converted from color space into grayscale image sized at 1024×1024 . The select step-by-step visualization of the Algorithm 2 is shown in Figure 6. The algorithm requires three parameters z^* , ω_c^* , m^* to be tuned as follows:

- z -axial PSF coordinate z^* used for the PSF model $h_{PSF}(z^*)$ defined in (1)
- Cutoff frequency ω_c^* used for setting the cutoff response of the MaxPol lowpass derivative basis filters
- Central moment m^* used for quantifying the m^{th} order energy of the focus feature vector

To tune these parameters, we performed a grid search to yield the best correlation accuracy between the subjective (ground-truth z -levels) and objective quality scores in our tuning database, which was a subset of full-FocusPath database introduced in [18].

In particular, the image patch is first decomposed (horizontally and vertically) using the HVS-M filter (see Figures 6(f) and 6(g)) and then exclude negative features with the ReLU function to avoid blurring adjacent features with redundant information (see Figures 6(d) and 6(e)). The feature map is vectorized and an adaptive proportion of the largest values are retained, using a nonlinear adaptive function (step 7), based on the 95th percentile of the feature vector's probability distribution function (PDF). The nonlinear function here determines the percentage of pixels to be selected from the original feature map (i.e. in step 9). This ensures that only the most dominant focus-relevant features are preserved, while ignoring the rest of the features that are mainly related to the noise artifacts. The offset threshold in step 7 is also tuned here on a small set of full FocusPath dataset which is not used during the experimental evaluations in order to claim its generalizability. In continue, the energy of the horizontal and vertical feature is taken in $\ell_{1/2}$ -norm space to promote feature sparsity along the horizontal and vertical directions (see Figure 6(b)). Finally, we calculate the m^{th} central moment of the most dominant values from the feature vector (see Figure

Algorithm 2: FQPath scoring of WSI patches

- Data:** Grayscale image patch $I \in \mathbb{R}^{N_1 \times N_2}$,
 Synthesized FIR kernel $h_{\text{HVS-M}}$,
 optimal parameter m^*
- Result:** Out-of-focus score $s \in \mathbb{R}$
- 1 Decompose grayscale image features using HVS-M
 $(F_x, F_y) = I * (h_{\text{HVS-M}}^T, h_{\text{HVS-M}})$
 - 2 Activate features
 $F_x^R = \max(F_x, 0), F_y^R = \max(F_y, 0)$
 - 3 Vectorize only positive features $v \equiv \text{vec}(F_x^{R+}, F_y^{R+})$
 - 4 Find 95th percentile of cumulative distribution function of the feature vector $\sigma_{0.95} = \text{CDF}(v, 95\%)$
 - 5 Find the proportion of features to be retained by
 $P = 0.25(1 - \tanh(60(\sigma_{0.95} - 0.095))) + 0.09$
 - 6 Find the #pixels to be retained $N_{\text{pix}} = PN_1N_2$
 - 7 Find the $\ell_{1/2}$ -norm feature vectors
 $F = \|(F_x^{R+}, F_y^{R+})\|_{\frac{1}{2}}$
 - 8 Retain $\bar{F} = \text{sort}_{\text{descend}}(F)_k, k \in \{1, \dots, N_{\text{pix}}\}$
 - 9 Calculate $\mu_{m^*} = \mathbb{E}[(\bar{F} - \mu_0)^{m^*}]$, where $\mu_0 = \mathbb{E}[\bar{F}]$
 - 10 Record the score value by $s = -\log \mu_{m^*}$

6(c)) and take its negative logarithm to obtain the final focus quality score. Note that the focus quality score is inversely proportional to the focus quality, i.e. a lower score indicates better focus quality.

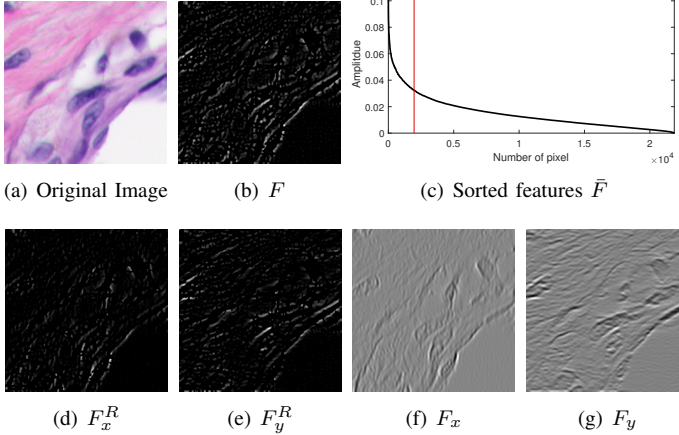


Fig. 6. Demo images after each single operation for metric analysis defined in Algorithm 2. The input image is decomposed by HVS-M kernel (d) horizontally and (e) vertically. The positive features are activated from both decomposed images shown in (f) and (g), where the superimposed feature map is shown in (b). The features are sorted in (c) and an adaptive threshold is applied to keep N_{pix} largest feature values.

IV. WSI-BASED LEVEL FOCUS QUALITY ASSESSMENT

Previously, we explained the focus quality measure at the WSI patch level, but for this measurement to be useful in a routine digital pathology workflow, it needs to be conducted at the tissue slide level. This way, the focus quality measure can be used to generate a local focus quality map (known as a heatmap) for an entire scanned slide. For a given whole slide image, we propose to divide it into patches of size 1024×1024

px, calculate the focus quality score for each patch separately, apply an inverse Gaussian projection (to linearize the focus quality gradation), and combine the patch scores into a slide-level focus quality heatmap. In this section, we describe the WSI database that we used for testing, our proposed inverse Gaussian projection linearization technique, and the subjective whole-slide scoring we conducted to validate our generated heatmaps.

A. Inverse Gaussian Projection

One additional step is used to prepare the patch-based focus quality measure discussed in the previous section for slide-level heatmap generation - inverse Gaussian projection. This ensures that the score-z profile (the relationship between the focus quality score and the known ground-truth z-level) is accurately linearized, which is important for proper visual perception of focus quality gradations and local extrema, since a non-linearized scale causes the heatmap to saturate near high and low focus quality values. We selected the inverse Gaussian projection to be the linearizing operation because we noticed that the score-z profiles tended to form an inverted Gaussian-like bell shape (as seen in Figures 7(a) and 7(c)).

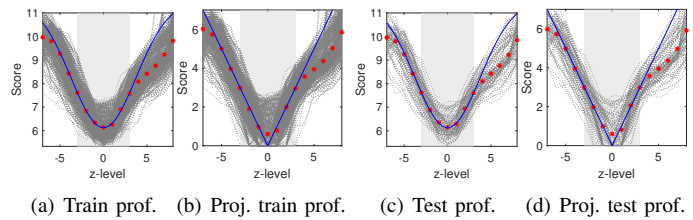


Fig. 7. Plots of z-profile scores, showing the individual profiles as grey dotted lines, the mean profiles as red asterisks, and the linear/Gaussian fits as blue solid lines, with the central grey region representing the fitting window: (a) Regular training z-profile scores, (b) Projected training z-profile scores, (c) Regular testing z-profile scores, (d) Projected testing z-profile scores

To implement and validate the inverse Gaussian projection, we take the full, unreleased version of the FocusPath database [18] ($540 \text{ lateral profiles} \times 16 \text{ z-levels} = 8640$ images in total) to be the training set for calibrating the projection, and a separate set of digital pathology images to be the test set ($90 \text{ lateral profiles} \times 16 \text{ z-levels} = 1440$ images in total) for validating the calibration. All profiles have ground-truth z-levels attached to them (integer values ranging from -7 to 8, inclusive). To train (or calibrate) the inverse Gaussian projection, we obtained the regular focus quality scores for these 540 training profiles, plotted them at their respective ground-truth z-levels, and found the mean focus quality score for each z-level (see the grey dotted lines and red asterisks respectively in Figure 7(a)). Then, we fitted a Gaussian $f(z) = ae^{-(z-b)^2/c}$ to the inverse mean focus quality score in the middle z-level values (i.e. the central grey region $z \in [-3, 3]$ in Figure 7(a)) to prioritize fitting in the high focus quality region (the optimal values were determined to be $a^* = 5.389, b^* = 0.005248, c^* = 5.301$). For testing, we first inverted the regular focus quality score, passed it through a threshold to ensure a non-negative argument to square root, and then applied the inverse of the fitted Gaussian to the score.

Algorithm 3: Inverse Gaussian projection on FQPath scores

Data: Training set of FQPath scores $s_t(n, z) \in \mathbb{R}$, where $n = \{1, \dots, 540\}$ and $z = \{1, \dots, 16\}$
Single test FQPath score $s \in \mathbb{R}$
Result: Projected testing FQPath score $s_p \in \mathbb{R}$

- 1 Find the mean train set profile $\bar{s}_t(z) = \mathbb{E}_n[s_t(n, z)]$
- 2 Calculate inverse mean profile
 $\bar{s}_{t,\text{inv}}(z) = \max(\bar{s}_t) - \bar{s}_t(z)$
- 3 Fit Gaussian model to inverse mean profile
 $\{a^*, b^*, c^*\} \leftarrow \underset{\{a,b,c\}}{\text{argmin}} \|\bar{s}_{t,\text{inv}}(z) - ae^{-(\frac{z-b}{c})^2}\|_2,$
where $z \in \{-3, -2, \dots, 2, 3\}$
- 4 Invert and threshold test set score
 $s_{\text{inv}} = \min(\max(\bar{s}_t) - s, a^*)$
- 5 Map test score by inverse Gauss.
 $s_p = c^* \sqrt{-\log \frac{s_{\text{inv}}}{a^*}} + b^*$

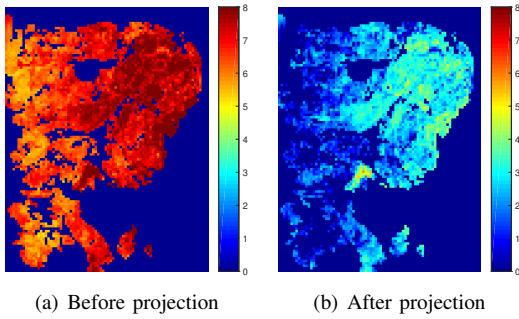


Fig. 8. Sample heatmap before and after projection. Note the greater visual saliency of low focus quality regions in the heatmap after projection. The range of colors denotes the value of the focus quality metric at each patch in a slide image, ranging from 0 to 8.

See algorithm 3 for details on the training and testing phases of the projection.

As can be seen in Figure 7, the score- z profiles are significantly more linear near inside the grey fitting window after projection (Figures 7(b) and 7(d)) than before projection (Figures 7(a) and 7(c)). Note that, in both the training and testing after-projection profiles, a minority of individual profiles undesirably stagnate near zero within the range $z \in [-2, 2]$. This is caused by the threshold operation required for the inverse Gaussian. When applied to an entire slide for heatmap generation, as shown in Figure 8, it is clear that the inverse Gaussian projection linearizes the heatmap colour scale, enabling better visual perception of focus quality gradations and local extrema.

B. 200-WSI Scan Database

For the purpose of focus quality assessment at the WSI level, we have collected a slide database consisting of 200 different WSIs scanned at 40X magnification ($0.25\mu\text{m}/\text{pixel}$ resolution) without compression using a TissueScope LE1.2 scanner. This database is selected from a larger set of 500 anonymized H&E tissue glass slides (sized $1'' \times 3''$, 1.0 mm in thickness) mainly provided by Southlake Regional Hospital and made available

to the authors courtesy of Huron Digital Pathology. The slides were specifically selected to cover the entire histopathological colour range and to exclude slides with excessive preparation imperfections, such as air bubbles and tissue folding. The tissue sections vary in thickness, organ of origin (e.g. brain, kidney, breast, liver, heart), and diagnosis (e.g. healthy, tuberculosis, cancer).

C. Subjective Whole-Slide Scoring

In order to validate the accuracy of the generated focus quality heatmaps, comparison must be made to a subjective score. Hence, we trained three human focus quality assessors to score the subjective quality of each slide at WSI-based level and compare these scores with the generated heatmaps. The assessors were trained on ground-truth views of in-focus and out-of-focus WSI regions displayed at 100% pixel resolution. A region was labeled “focus-rejected” when more than half of the screen view area was out-of-focus. Accordingly, the following procedure was followed:

- 1) Open the WSI in the HuronViewer program ⁴
- 2) Increase the zoom level to 100% pixel resolution
- 3) Using the thumbnail view, mentally plan the slide navigation pattern prior to the commencement of the slide navigation for assessment points to cover as much of the tissue regions and as evenly as possible (for example see Figure 9 (left plot)).
- 4) Start a one-minute countdown within view of the slide
- 5) Using the thumbnail view, navigate the field of view to the first assessment point
- 6) Determine the field-of-view (FOV) around the first assessment point to be in-focus (pass) or out-of-focus (fail)
- 7) Increment the count of passing and failing focus quality assessment points accordingly
- 8) Proceed to the next assessment point (according to the pre-planned slide navigation pattern) and repeat steps 6 to 8 until either one minute has passed or the pre-planned slide navigation pattern has been completed early

The one-minute countdown used here was simply an online countdown app that was started within view of the slide on a computer monitor. Any similar setup could be used which enables the assessor to easily see the remaining time without obscuring the slide.

As a result, each of the 200 slides was assigned two numbers (pass and fail counts) by the three assessors and an acceptance ratio (number of pass points divided by total points) was calculated from these counts. The statistical distribution of the slide acceptance ratios in the 200-WSI database is shown in Figure 9 (right plot).

The set of 200 slides contain large number of out-of-focus slides (almost one third of the whole set) that have been fairly detected by two assessors, yielding with low acceptance ratio. Note the great difference between the third subject and the other two (i.e. Subject #1 and #2). This is because the third subject assigned higher acceptance rate toward the out-of-focus slides. In fact, this shows the assessor subjective scores differ

⁴HuronViewer is freely available at <http://www.hurondigitalpathology.com/resources/>

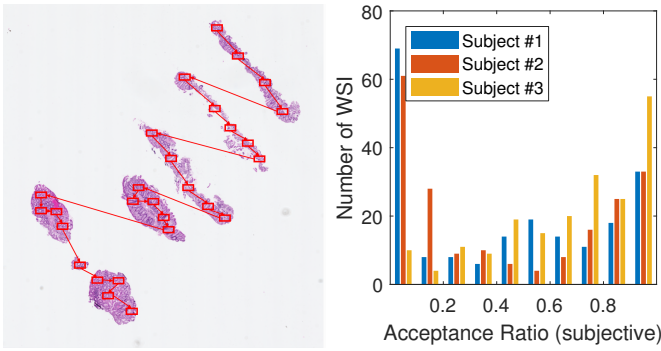


Fig. 9. Left plot: Sample pre-planned navigation pattern of assessment points through a slide. The assessor navigates through different positions within the tissue thumbnail at 100% image resolution and records each as pass/fail. The ratio of pass points to total points determines the acceptance ratio of WSI sharpness. Right plot: Statistical distribution of acceptance ratio across 200 WSI database and three different subjective ratings.

due to their varying expertise and quality criteria.. One can obtain the mean opinion score (as is standard practice in image quality assessment [41], [42]) to create the relative subjective scoring of the whole slide image.

V. EXPERIMENT NO.1: PATCH-LEVEL ANALYSIS

In this section, we describe the design, implementation and execution of several experiments at the WSI patch level to evaluate our proposed FQ metric in terms of accuracy, processing speed, computational complexity, and image compression analysis. We compare our metric against 10 state-of-the-art NR-FQA metrics, including S₃ [43], MLV [5], ARISM_C [44], GPC [14], SPARISH [6], RISE [8], MaxPol [36], HVS-1 and HVS-2 [18], and MIFQ [33].

A. Performance Evaluation

We perform the accuracy analysis on the regular version of the digital pathology database FocusPath⁵ introduced in [18]. The database contains 864 naturally-blurred patches (sized 1024×1024 px) extracted from whole-slide scans. The MIFQ measure, by default, operates on patches sized 84×84 (a variant of deep-learning solution). For a fair comparison each FocusPath patch was divided into 84×84 smaller patches and their average was computed as the overall patch-level focus score.

All 11 candidate metrics are assessed to determine their correlation with the known ground-truth *z*-level of each patch, which is measured using the Pearson linear correlation coefficient (PLCC), Spearman rank order correlation (SRCC), Kendall rank correlation coefficient (KRCC) and root mean square error (RMSE). For more information on these four accuracy measures, please refer to [41], [42]. PLCC measures linear correlation, SRCC measures the strength and direction of monotonicity, KRCC indicates the ordinal association, and RMSE measures the difference in value. we conduct further analysis on the performances of different NR-FQA metrics using the statistical analysis method introduced in [45], [46].

In particular, we deploy the statistical significance analysis on the objective quality assessments using three different measurements of Area Under the Curve (AUC) of the Receiver Operating Characteristic (ROC) to (a) distinguish between different and similar objective pairs AUC_{DS}, (b) recognize the stimulus of higher objective quality within significantly different pair AUC_{BW}, and evaluate the percentage of correct classification rate of a metric C₀. The latter evaluation benchmark creates a meaningful way of comparison by transforming the values of focus depth (which are treated as subjective scores for ground truth scoring) into binary sets of better/worse, and different/similar that is less invariant toward the amplitude scoring [45], [46]. The results of the performance accuracies are provided in Table I. The top-three NR-FQAs here are FQPath, HVS-MaxPol-2, and MLV (shown in bold numeric). The average calculation time (speed) of all methods are also shown in the same table, where among all three top methods, FQPath is twice and four times faster than HVS-MaxPol-2 and MLV, respectively. Furthermore, when the scores are plotted relative to the absolute value of the ground-truth *z*-levels, as in Figure 10, it is clear that FQPath is by far the most correlated with the ground-truth.

B. Statistical Significance Test

The results of statistical significance tests are also shown in Table II across different NR-FQAs by calculating the critical ratio between AUCs defined in [45]. Here, 95% confidence interval is used to determine the significance over the statistical distribution. The Green square indicates the metric across the row is significantly better than the metric across the column. Whereas, the red square indicates the opposite. There are no statistical significance observed over the black squares. The results indicate that FQPath is significantly better than the other ten NR-FQAs over AUC_{BW} yielding higher sensitivity toward recognizing the out-of-focus stimuli. We also observe that FQPath is significantly equal to HVS-MaxPol-2 and MLV across AUC_{DS} and C₀. Furthermore, we evaluate the overall significance of each NR-FQA by accumulating the number of inferior (-1)/equal (0)/significant (+1) across all competing methods. The results are shown in Table I under three different AUC categories. Note that the proposed FQPath outranks all the competing methods with respect to three different significance criteria. In parcticular, FQPath is not inferior with respect to any other methods, while all the other competing methods yields at least one inferiority across all three categories. Also, note that FQPath remains 28 times superior across all three categories, succeeding the second best method i.e. HVS-MaxPol-2 which is 26.

C. Computational Complexity Analysis

Another characteristic of a good focus quality metric for digital pathology is a low computational complexity, since digital pathology images are usually extremely large in size. For example, a 1cm×1cm tissue specimen scanned at 40X resolution is 4.8 GB in size. We designed and executed two experiments for computational complexity analysis: (1) to compare the times required by the competing metrics for

⁵<https://sites.google.com/view/focuspathuoft>

TABLE I

PLCC, SRCC, KRCC, AND RMSE PERFORMANCE OF DIFFERENT FQA METRICS ON FOCUSPATH DATABASE. THE TOP THREE METRICS FOR EACH ACCURACY MEASURE ARE SHOWN IN BOLD. THE STATISTICAL SIGNIFICANCE (SS) OF PLCC, SRCC, AND KRCC ACCURACY RESULTS ARE ALSO SHOWN ON RIGHT COLUMN. '+1' INDICATES THAT FQPATH IS SIGNIFICANTLY MORE ACCURATE, '-1' INDICATES FQPATH IS SIGNIFICANTLY LESS ACCURATE, AND '0' INDICATES THAT THERE IS NO SIGNIFICANT DIFFERENCE.

	PLCC	SRCC	KRCC	RMSE	AUC _{DS}	AUC _{BW}	C ₀	#Sig _{DS}	#Sig _{BW}	#Sig _{C₀}	Time (sec)
	-1	0	+1	-1	0	+1	-1	0	+1	-1	
S ₃ [43]	0.7969	0.7957	0.6205	1.4928	0.7119	0.9834	0.9279	5	0	5	50.1140
MLV [5]	0.8569	0.8636	0.6988	1.2737	0.7664	0.9929	0.9662	2	1	7	0.2146
ARISM _C [44]	0.2263	0.3043	0.2195	2.4068	0.5394	0.6856	0.6645	10	0	0	55.4629
GPC [14]	0.7499	0.7811	0.6020	1.6346	0.6310	0.9703	0.9235	8	0	2	0.2400
SPARISH [6]	0.3459	0.3566	0.2626	2.3184	0.5821	0.6620	0.6377	9	0	1	8.4285
RISE [8]	0.6509	0.6566	0.4903	1.8758	0.6543	0.9179	0.8442	7	0	3	3.6969
MaxPol [36]	0.7058	0.7176	0.5897	1.7504	0.6716	0.9309	0.6565	6	0	4	0.2907
HVS-MaxPol-1 [18]	0.8212	0.8144	0.6383	1.4100	0.7561	0.9841	0.9343	4	0	6	0.0560
HVS-MaxPol-2 [18]	0.8538	0.8574	0.6852	1.2865	0.8101	0.9948	0.9621	0	1	9	0.1100
MIFQ [33]	0.8286	0.8200	0.6397	1.3834	0.7656	0.9905	0.9398	2	1	7	N/A
FQPath (proposed)	0.8556	0.8606	0.6888	1.2789	0.8101	0.9954	0.9657	0	1	9	0.0598

TABLE II

THE RESULTS OF STATISTICAL SIGNIFICANCE ANALYSIS ON FOCUSPATH DATABASE. THE GREEN CELL INDICATES THAT THE NR-FQA METRIC IN THE ROW OUTPERFORMS THE METRIC IN THE COLUMN, AND THE RED CELL SHOWS THE OPPOSITE. THE BLACK CELL SHOWS THAT THE METRICS IN THE ROW AND COLUMN ARE COMPARABLE.

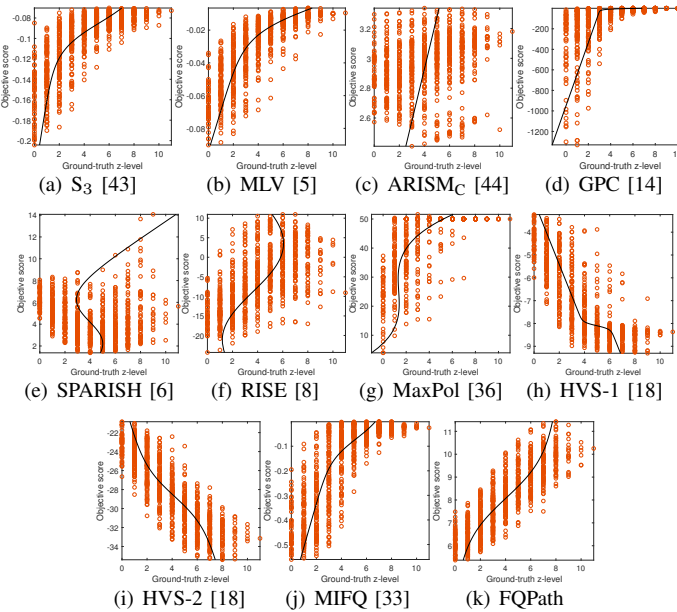
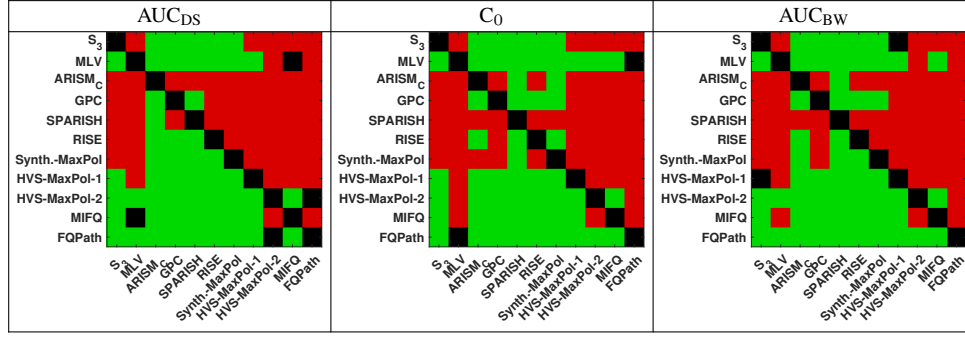


Fig. 10. Plots of each competing focus score with the absolute value of their associated ground-truth z-level for each image patch in FocusPath. Note how the plot for FQPath shows a consistent linear trend between z-level and score which is not paralleled by the other metrics.

images of different sizes, and (2) to compare the competing metrics by their PLCC accuracy and their run-time per pixel (on 2048×2048 images). Both experiments are done on a Windows station with an AMD FX-8370E 8-Core CPU 3.30 GHz.

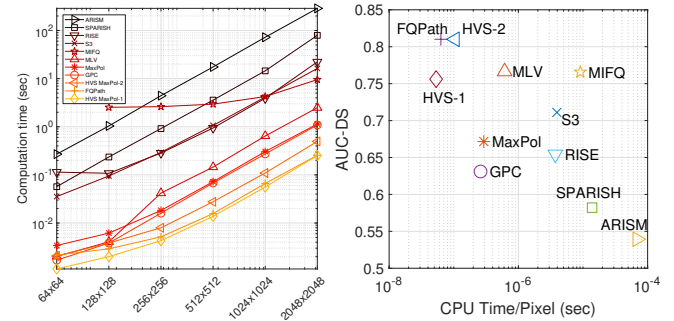


Fig. 11. Left plot: Computational complexity analysis using run time vs. image size for different FQ methods. Right plot: AUC_{DS} vs. run time per pixel using different methods. Ideal methods (high accuracy, high computational speed) are found at the top-left corner.

Figure 11 (left plot) demonstrates the computational complexity of all 11 FQ metrics with respect to different image sizes. We selected 20 sample images of different patch sizes i.e. {64, 128, 256, 512, 1024, 2048} and average the CPU time over all 20 trials to report the computation time. Note that the test rank of HVS-MaxPol-1 and FQPath are consistent over different image sizes. For a 1024 × 1024 patch, FQPath takes

0.06626 s, HVS-MaxPol-2 takes double the time (0.1905 s), and MIFQ takes 74 times (4.234 s).

Figure 11 (right plot) demonstrates the relationship between AUC_{DS} performance and CPU run time. A large y- (vertical) axis value indicates high accuracy performance and low x- (horizontal) axis value indicates high speed. Therefore, an ideal method would be located at the top-left corner, such as FQPath, HVS-MaxPol-1, and HVS-MaxPol-2. Overall, FQPath performs excellently in terms of both accuracy and speed, proving to be highly reliable for digital pathology FQ assessment.

D. Image Compression Analysis

WSI scan size in digital pathology scanned at high image resolution are very large in raw format (TIFF) that creates huge challenges for storing, processing, and communication. This is usually addressed by employing lossy compression image converters such as JPEG2000. However, such lossy compression image formatting introduces artifacts such as block artifacts and blurring. Our aim here is to assess the focus quality metric on compressed image scans to determine the suitability of the methodology in the common scenario where WSIs are not in raw format. Figure 12 demonstrates the correlation accuracy of the FQPath metric on different focus levels of FocusPath database using different compression ratio factors. The results demonstrate how the proposed methodology maintains its robustness toward quantifying the amount of image degradation due to focus blur and compression loss.

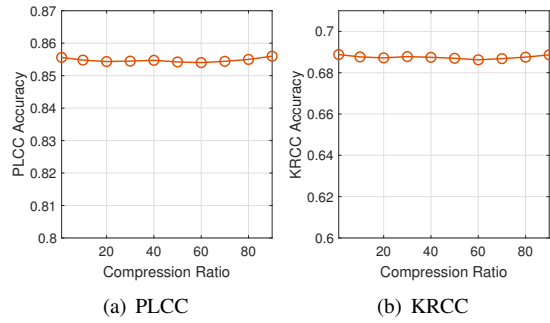


Fig. 12. JPEG2000 compression analysis of FQPath using FocusPath dataset with respect to different compression ratios.

VI. EXPERIMENT NO.2: WSI-LEVEL ANALYSIS

At the whole-slide level, FQPath can be applied (with the inverse Gaussian projection) to construct a slide focus quality heatmap and visualize the regions of high and low focus quality. In this section, we propose two experiments to show the validity of our approach to whole-slide-level focus quality assessment: (1) display the FQ heatmaps generated for some select whole slide images, and (2) correlate the FQ heatmaps with the subjective slide quality scores.

A. Heat Map Analysis

In Figure 13, we show the focus quality heatmaps generated for 12 select slides. The shade of colors in heatmaps are demonstrated from blue to red corresponding from low to

high focus quality, respectively. Note how local regions of low focus quality are easily visible in shades of blue and cyan. The distribution of patch quality scores in these focus quality heatmaps is indicative of overall scan quality and decide whether to accept or reject the scan.

In particular, note the banding in Slides 1, 3, 6, and 10 which is due to uneven focus across the field of view. Similar banding effect in Slide 2 can be also found on the three mouse brains on the left. This was caused by tilting the sample in the xz-plane about the y-axis and is indeed an indication that the setup was sub-optimal. In the thumbnail images of Slides 1, 3, 6, and 10 we can see that the illumination is quite even. In fact, it is readily evident that in Slides 4 and 11 the illumination is uneven (smear of shadows in multiple strips) but the focus quality metric is not sensitive to this (compare slide 4's focus quality map with that of 1 and 3 – almost no banding despite the obvious illumination unevenness). It is also noteworthy that, from signal processing viewpoint, the distribution of such uneven illumination is manifested as very-low frequency distribution on the image spectrum. This can be treated as almost biased signal levels on limited region of interest (small patch area). By applying the convolution kernel HVS-M in Step-3 in Algorithm 2 on the image scan for focus quality measurements, such bias artifacts will be almost eliminated as the decomposing kernel HVS-M is constructed by the combination of multiple derivative orders (see Equation 4).

In Table III, we show example patches for each of five histogram bins for each heatmap. Note how the patches vary in focus quality from crisp tissue scans to increasing degrees of blur. This supports the validity of our proposed focus quality heatmap where the processing metric provides a reliable and robust analysis of focus measures within intraclass and interclass of tissue types across different slide images.

B. Subjective Whole-Slide Scoring

In order to correlate our FQ heatmaps with our subjective slide quality scores, we considered the heatmap patch quality scores independently and generated cumulative summation curves to determine their distribution. In Figure 13 (last row), we show these cumulative summation curves for five different WSIs. In Figures 14 (left plot) we show the PLCC between the heatmap scores with the subjective slide scores, and determined the optimal heatmap score threshold to be 1.7688 based on the PLCC plot. And in Figure 14 (right plot), we plot the optimally-thresholded heatmap acceptance ratio with the subjective slide scores. We fit the data using the non-linear regression model from [42]. The objective heatmap acceptance ratio here forms a monotone response with respect to the subjective acceptance ratio. The corresponding correlation accuracy measurements are provided in Table IV indicating the feasibility of using FQPath for slide-level quality control.

VII. CONCLUSION

The concluding remarks of this paper are listed in the following paragraphs.

In this paper we have presented an accurate and computationally efficient automated no-reference focus quality

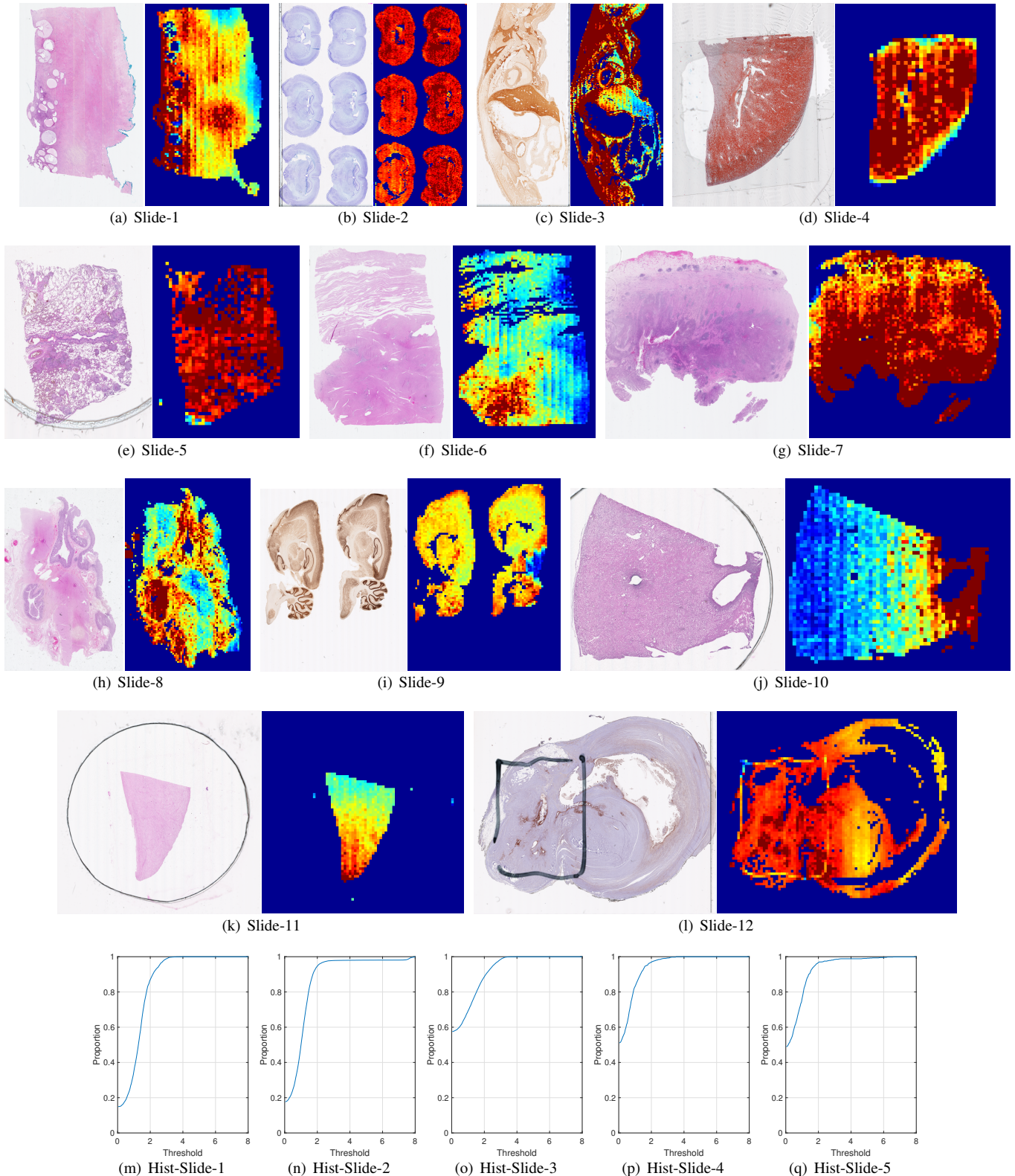


Fig. 13. Raw pyramid images and their focus quality heatmaps shown from (a)-(l). The corresponding heatmap score cumulative summation curves for Slides (a)-(e) are also shown from (m) to (q), respectively, where faster-rising curves indicating better overall slide quality. A 10-bin histogram of all the heatmaps is taken and one example patch taken from each bin of the slide (indicated by the red arrows, with larger bin numbers indicating better focus quality). See the patches themselves inside Figure III.

TABLE III
EXAMPLE IMAGE PATCHES FROM FIVE SLIDE IMAGES.

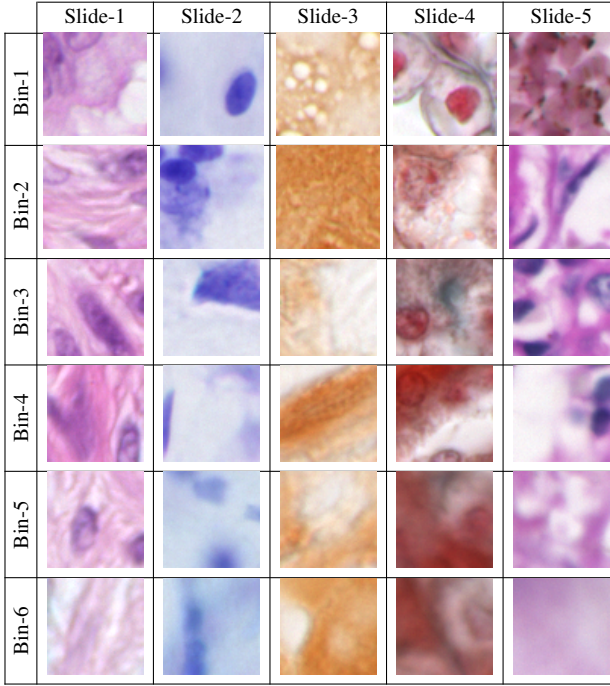


TABLE IV
PLCC, SRCC, AND KRCC CORRELATION ACCURACY PERFORMANCE
BETWEEN OBJECTIVE ACCEPTANCE RATIO AND SUBJECTIVE ACCEPTANCE
RATIO ACROSS 200 WSI SCANS.

PLCC	SRCC	KRCC
0.79569	0.51826	0.37184

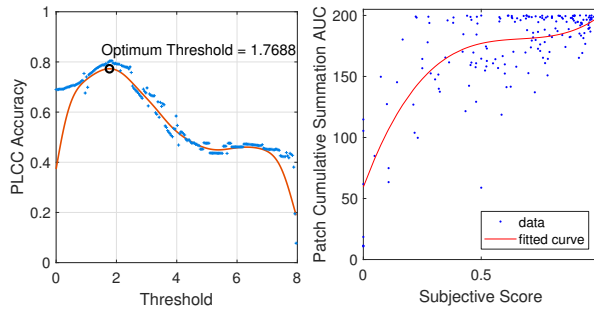


Fig. 14. Left plot: PLCC across different threshold values, between the slide-level FQPath objective score and the subjective acceptance ratio. Smoothed plot shown as solid line with objective acceptance threshold of 1.7688 that maximizes correlation between the objective and subjective slide-level acceptance ratio. Right plot: Objective Acceptance Ratio (using acceptance threshold of 1.7688) vs. Subjective Acceptance Ratio. Red line indicates IQA fit through data

assessment (NR-FQA) technique that is currently needed for digital pathology workflows. It provides a practical solution for high-throughput scanning tasks that can be utilized in both image patch (aka block) and whole slide image (WSI) levels for focus quality evaluation of image scans. The method estimates the point spread function corresponding to the out-of-focus of the scanner imaging optics and synthesizes its inverse response as a sum of even-derivative filter bases. This kernel behaves similarly to the human visual system by modifying attenuated high-frequency image information. A set of digital pathology images are convolved with this synthesized filter to extract focus quality-related features and quantified these features to determine the quality score. The accuracy and computational efficiency of the proposed method are demonstrated in two fold: (a) the metric is evaluated at patch level and compared to ten other state-of-the-art NR-FQA metrics; and (b) the application of the proposed metric is demonstrated at WSI level to generate local focus quality maps (heatmaps), which are showed to be usable for automatically quantifying a slide's overall focus quality.

The proposed NR-FQA metric retains both accuracy and speed that can favorably extended in different medical imaging applications for better engineering of QC control in helping clinicians/physicians to better serve the public health. Modalities include but not limited to brightfield microscopy, darkfield microscopy, fluorescence microscopy, confocal microscopy, etc. The metric could also be used to analyze the relevance of out-of-focus for developing automated diagnosis tools that have recently gained attention in computational pathology [47]–[49].

Scanners are designed to optimize the balance between speed and image sharpness so the sampling will stay close to the Nyquist limit. This means the optical parameters and digitization parameters stay relatively fixed for this application, which is an advantage. However, they are not fixed absolutely – they can vary slightly between scanner designs by maybe a factor of 2 (even much less), especially between those that use a monochrome sensor and pulsed colour illumination versus those that use a CFA colour sensor with white light illumination, since the pixel pitch needs to be tighter in the latter case. The comparison between these methods is the most interesting and straying too far from the idealized Nyquist limit is not very useful from an application point of view, however interesting it may be from an algorithm performance or scientific point of view.

furthermore, the idealized PSF assumed in this paper does not differ between positive and negative defocus. The point of using a model PSF is that it approximates the defocus with minimal perturbations. A refinement could be to use a “real” PSF or models that account for aberrations, etc.

VIII. ACKNOWLEDGMENT

The authors would like to greatly thank Huron Digital Pathology, for providing valuable discussion and a database for developing the experiments conducted in this paper. The first, second, and third authors’ research was partially supported by an NSERC Collaborative Research and Development Grant (contract CRDPJ-486583-15).

REFERENCES

- [1] Victor Sanchez and Miguel Hernández-Cabronero, "Graph-based rate control in pathology imaging with lossless region of interest coding," *IEEE Transactions on Medical Imaging*, 2018.
- [2] Liron Pantanowitz, Paul N Valenstein, Andrew J Evans, Keith J Kaplan, John D Pfeifer, David C Wilbur, Laura C Collins, and Terence J Colgan, "Review of the current state of whole slide imaging in pathology," *Journal of pathology informatics*, vol. 2, 2011.
- [3] Navid Farahani, Anil V Parwani, and Liron Pantanowitz, "Whole slide imaging in pathology: advantages, limitations, and emerging perspectives," *Pathol Lab Med Int*, vol. 7, pp. 23–33, 2015.
- [4] Gloria Bueno, M Milagro Fernández-Carrobles, Oscar Deniz, and Marcial García-Rojo, "New trends of emerging technologies in digital pathology," *Pathobiology*, vol. 83, no. 2-3, pp. 61–69, 2016.
- [5] Khosro Bahrami and Alex C. Kot, "A fast approach for no-reference image sharpness assessment based on maximum local variation," *IEEE Signal Processing Letters*, vol. 21, no. 6, pp. 751–755, 2014.
- [6] Leida Li, Dong Wu, Jinjian Wu, Haoliang Li, Weisi Lin, and Alex C. Kot, "Image sharpness assessment by sparse representation," *IEEE Transactions on Multimedia*, vol. 18, no. 6, pp. 1085–1097, 2016.
- [7] Leida Li, Weisi Lin, Xuesong Wang, Gaobo Yang, Khosro Bahrami, and Alex C. Kot, "No-reference image blur assessment based on discrete orthogonal moments," *IEEE Transactions on Cybernetics*, vol. 46, no. 1, pp. 39–50, 2016.
- [8] Leida Li, Wenhua Xia, Weisi Lin, Yuming Fang, and Shiqi Wang, "No-reference and robust image sharpness evaluation based on multiscale spatial and spectral features," *IEEE Transactions on Multimedia*, vol. 19, no. 5, pp. 1030–1040, 2017.
- [9] Yutao Liu, Ke Gu, Guangtao Zhai, Xianming Liu, Debin Zhao, and Wen Gao, "Quality assessment for real out-of-focus blurred images," *Journal of Visual Communication and Image Representation*, vol. 46, pp. 70–80, 2017.
- [10] Anmin Liu, Weisi Lin, and Manish Narwaria, "Image quality assessment based on gradient similarity," *IEEE Transactions on Image Processing*, vol. 21, no. 4, pp. 1500–1512, 2012.
- [11] Jingwei Guan, Wei Zhang, Jason Gu, and Hongliang Ren, "No-reference blur assessment based on edge modeling," *Journal of Visual Communication and Image Representation*, vol. 29, pp. 1–7, 2015.
- [12] Goran Gvozden, Sonja Grgic, and Mislav Grgic, "Blind image sharpness assessment based on local contrast map statistics," *Journal of Visual Communication and Image Representation*, vol. 50, pp. 145–158, 2018.
- [13] Rania Hassen, Zhou Wang, and Magdy M. A. Salama, "Image sharpness assessment based on local phase coherence," *IEEE Transactions on Image Processing*, vol. 22, no. 7, pp. 2798–2810, 2013.
- [14] Arthur Leclaire and Lionel Moisan, "No-reference image quality assessment and blind deblurring with sharpness metrics exploiting Fourier phase information," *Journal of Mathematical Imaging and Vision*, vol. 52, no. 1, pp. 145–172, 2015.
- [15] Le Kang, Peng Ye, Yi Li, and David Doermann, "Convolutional neural networks for no-reference image quality assessment," in *Proceedings of the IEEE Conference on Computer Vision and Pattern Recognition*, 2014, pp. 1733–1740.
- [16] Shaode Yu, Fan Jiang, Leida Li, and Yaoqin Xi, "Cnn-grnn for image sharpness assessment," in *Asian Conference on Computer Vision*. Springer, 2016, pp. 50–61.
- [17] Shaode Yu, Shibin Wu, Lei Wang, Fan Jiang, Yaoqin Xie, and Leida Li, "A shallow convolutional neural network for blind image sharpness assessment," *PloS One*, vol. 12, no. 5, pp. e0176632, 2017.
- [18] M. S. Hosseini, Y. Zhang, and K. N. Plataniotis, "Encoding visual sensitivity by maxpol convolution filters for image sharpness assessment," *IEEE Transactions on Image Processing*, pp. 1–1, 2019.
- [19] Rafael Redondo, Gabriel Cristóbal, Gloria Bueno García, Oscar Deniz, Jesus Salido, Maria del Milagro Fernandez, Juan Vidal, Juan Carlos Valdviezo, Rodrigo Nava, Boris Escalante-Ramírez, et al., "Autofocus evaluation for brightfield microscopy pathology," *Journal of biomedical optics*, vol. 17, no. 3, pp. 036008, 2012.
- [20] Xavier Moles Lopez, Etienne D'Andrea, Paul Barbot, Anne-Sophie Bridoux, Sandrine Rorive, Isabelle Salmon, Olivier Debeir, and Christine Decaestecker, "An automated blur detection method for histological whole slide imaging," *PloS one*, vol. 8, no. 12, pp. e82710, 2013.
- [21] Maria João M Vasconcelos and Luís Rosado, "No-reference blur assessment of dermatological images acquired via mobile devices," in *International Conference on Image and Signal Processing*. Springer, 2014, pp. 350–357.
- [22] Ana Jiménez, Gloria Bueno, Gabriel Cristóbal, Oscar Déniz, David Toomey, and Catherine Conway, "Image quality metrics applied to digital pathology," in *Optics, Photonics and Digital Technologies for Imaging Applications IV*. International Society for Optics and Photonics, 2016, vol. 9896, p. 98960S.
- [23] Sami Koho, Elnaz Fazeli, John E Eriksson, and Pekka E Hänninen, "Image quality ranking method for microscopy," *Scientific reports*, vol. 6, pp. 28962, 2016.
- [24] Alma Rocío Cabazos-Marín and Josué Álvarez-Borrego, "Automatic focus and fusion image algorithm using nonlinear correlation: Image quality evaluation," *Optik*, vol. 164, pp. 224–242, 2018.
- [25] Román Hurtado-Pérez, Carina Toxqui-Quitl, Alfonso Padilla-Vivanco, J. Félix Aguilar-Valdez, and Gabriel Ortega-Mendoza, "Focus measure method based on the modulus of the gradient of the color planes for digital microscopy," *Optical Engineering*, vol. 57, no. 2, pp. 023106, 2018.
- [26] Gabriele Campanella, Arjun R Rajanna, Lorraine Corsale, Peter J Schüffler, Yukako Yagi, and Thomas J Fuchs, "Towards machine learned quality control: A benchmark for sharpness quantification in digital pathology," *Computerized Medical Imaging and Graphics*, vol. 65, pp. 142–151, 2018.
- [27] Bas Hulskens, "Autofocus based on differential measurements," Nov. 28 2017, US Patent 9,832,365.
- [28] Michael C Montalto, Richard R McKay, and Robert J Filkins, "Autofocus methods of whole slide imaging systems and the introduction of a second-generation independent dual sensor scanning method," *Journal of pathology informatics*, vol. 2, 2011.
- [29] Shaowei Jiang, Jun Liao, Zichao Bian, Kaikai Guo, Yongbing Zhang, and Guoan Zheng, "Transform-and multi-domain deep learning for single-frame rapid autofocusing in whole slide imaging," *Biomedical optics express*, vol. 9, no. 4, pp. 1601–1612, 2018.
- [30] Mark-Anthony Bray, Adam N Fraser, Thomas P Hasaka, and Anne E Carpenter, "Workflow and metrics for image quality control in large-scale high-content screens," *Journal of biomolecular screening*, vol. 17, no. 2, pp. 266–274, 2012.
- [31] Bernd Lahmann, Nektarios A Valous, Urs Eisenmann, Nicolas Wentzensen, and Niels Grabe, "Semantic focusing allows fully automated single-layer slide scanning of cervical cytology slides," *PloS one*, vol. 8, no. 4, pp. e61441, 2013.
- [32] Mark-Anthony Bray and Anne E Carpenter, "Quality control for high-throughput imaging experiments using machine learning in cellprofiler," in *High Content Screening*, pp. 89–112. Springer, 2018.
- [33] Samuel J Yang, Marc Berndl, D Michael Ando, Mariya Barch, Arunachalam Narayanasamy, Eric Christiansen, Stephan Hoyer, Chris Roat, Jane Hung, Curtis T Rueden, et al., "Assessing microscope image focus quality with deep learning," *BMC bioinformatics*, vol. 19, no. 1, pp. 77, 2018.
- [34] M. S. Hosseini and K. N. Plataniotis, "Derivative kernels: Numerics and applications," *IEEE Transactions on Image Processing*, vol. 26, no. 10, pp. 4596–4611, Oct 2017.
- [35] Mahdi S. Hosseini and Konstantinos N. Plataniotis, "Finite differences in forward and inverse imaging problems: Maxpol design," *SIAM Journal on Imaging Sciences*, vol. 10, no. 4, pp. 1963–1996, 2017.
- [36] Mahdi S Hosseini and Konstantinos N Plataniotis, "Image sharpness metric based on maxpol convolution kernels," in *2018 25th IEEE International Conference on Image Processing (ICIP)*. IEEE, 2018, pp. 296–300.
- [37] Max Born and Emil Wolf, *Principles of optics: electromagnetic theory of propagation, interference and diffraction of light*, Elsevier, 2013.
- [38] David J. Field, "Relations between the statistics of natural images and the response properties of cortical cells," *Josa a*, vol. 4, no. 12, pp. 2379–2394, 1987.
- [39] Nuala Brady and David J. Field, "What's constant in contrast constancy? the effects of scaling on the perceived contrast of bandpass patterns," *Vision Research*, vol. 35, no. 6, pp. 739–756, 1995.
- [40] David J. Field and Nuala Brady, "Visual sensitivity, blur and the sources of variability in the amplitude spectra of natural scenes," *Vision Research*, vol. 37, no. 23, pp. 3367–3383, 1997.
- [41] Zhou Wang, A.C. Bovik, H.R. Sheikh, and E.P. Simoncelli, "Image quality assessment: From error visibility to structural similarity," *IEEE Transactions on Image Processing*, vol. 13, no. 4, pp. 600–612, 2004.
- [42] H.R. Sheikh, M.F. Sabir, and A.C. Bovik, "A statistical evaluation of recent full reference image quality assessment algorithms," *IEEE Transactions on Image Processing*, vol. 15, no. 11, pp. 3440–3451, 2006.
- [43] Vu CT, Phan TD, and Chandler DM, "S₃: A spectral and spatial measure of local perceived sharpness in natural images," *IEEE Transactions on Image Processing*, vol. 21, no. 3, pp. 934–945, 2012.

- [44] Ke Gu, Guangtao Zhai, Weisi Lin, Xiaokang Yang, and Wenjun Zhang, “No-reference image sharpness assessment in autoregressive parameter space,” *IEEE Transactions on Image Processing*, vol. 24, no. 10, pp. 3218–3231, 2015.
- [45] Lukáš Krasula, Karel Fliegel, Patrick Le Callet, and Miloš Klíma, “On the accuracy of objective image and video quality models: New methodology for performance evaluation,” in *Quality of Multimedia Experience (QoMEX), 2016 Eighth International Conference on*. IEEE, 2016, pp. 1–6.
- [46] Lukáš Krasula, Patrick Le Callet, Karel Fliegel, and Miloš Klíma, “Quality assessment of sharpened images: Challenges, methodology, and objective metrics,” *IEEE Transactions on Image Processing*, vol. 26, no. 3, pp. 1496–1508, 2017.
- [47] Can Taylan Sari and Cigdem Gunduz-Demir, “Unsupervised feature extraction via deep learning for histopathological classification of colon tissue images,” *IEEE transactions on medical imaging*, 2018.
- [48] Caner Mercan, Selim Aksoy, Ezgi Mercan, Linda G Shapiro, Donald L Weaver, and Joann G Elmore, “Multi-instance multi-label learning for multi-class classification of whole slide breast histopathology images,” *IEEE transactions on medical imaging*, vol. 37, no. 1, pp. 316–325, 2018.
- [49] Jon N Marsh, Matthew K Matlock, Satoru Kudose, Ta-Chiang Liu, Thaddeus S Stappenbeck, Joseph P Gaut, and S Joshua Swamidass, “Deep learning global glomerulosclerosis in transplant kidney frozen sections,” *bioRxiv*, p. 292789, 2018.